



A Framework for Multiphase Galactic Wind Launching Using TIGRESS

Chang-Goo Kim^{1,2}, Eve C. Ostriker¹, Drummond B. Fielding², Matthew C. Smith^{2,3}, Greg L. Bryan^{2,4},
Rachel S. Somerville^{2,5}, John C. Forbes², Shy Genel^{2,6}, and Lars Hernquist³

¹ Department of Astrophysical Sciences, Princeton University, 4 Ivy Lane, Princeton, NJ 08544, USA; cgkim@astro.princeton.edu

² Center for Computational Astrophysics, Flatiron Institute, 162 Fifth Avenue, New York, NY 10010, USA

³ Harvard-Smithsonian Center for Astrophysics, 60 Garden Street, Cambridge, MA 02138, USA

⁴ Department of Astronomy, Columbia University, 550 West 120th Street, New York, NY 10027, USA

⁵ Department of Physics and Astronomy, Rutgers University, 136 Frelinghuysen Rd, Piscataway, NJ 08854, USA

⁶ Columbia Astrophysics Laboratory, Columbia University, 550 West 120th Street, New York, NY 10027, USA

Received 2020 September 10; revised 2020 October 13; accepted 2020 October 16; published 2020 November 9

Abstract

Galactic outflows have density, temperature, and velocity variations at least as large as those of the multiphase, turbulent interstellar medium (ISM) from which they originate. We have conducted a suite of parsec-resolution numerical simulations using the TIGRESS framework, in which outflows emerge as a consequence of interaction between supernovae (SNe) and the star-forming ISM. The outflowing gas is characterized by two distinct thermal phases, cool ($T \lesssim 10^4$ K) and hot ($T \gtrsim 10^6$ K), with most mass carried by the cool phase and most energy and newly injected metals carried by the hot phase. Both components have a broad distribution of outflow velocity, and especially for cool gas this implies a varying fraction of escaping material depending on the halo potential. Informed by the TIGRESS results, we develop straightforward analytic formulae for the joint probability density functions (PDFs) of mass, momentum, energy, and metal loading as distributions in outflow velocity and sound speed. The model PDFs have only two parameters, star formation rate surface density Σ_{SFR} and the metallicity of the ISM, and fully capture the behavior of the original TIGRESS simulation PDFs over $\Sigma_{\text{SFR}} \in (10^{-4}, 1) M_{\odot} \text{ kpc}^{-2} \text{ yr}^{-1}$. Employing PDFs from resolved simulations will enable implementations of subgrid models for galaxy formation with wind velocity and temperature (as well as total loading factors) that are based on theoretical predictions rather than empirical tuning. This is a critical step to incorporate advances from TIGRESS and other high-resolution simulations in future cosmological hydrodynamics and semi-analytic galaxy formation models. We release a Python package to prototype our model and to ease its implementation.

Unified Astronomy Thesaurus concepts: [Galactic winds \(572\)](#); [Galaxy winds \(626\)](#); [Galaxy fountains \(596\)](#); [Galaxy formation \(595\)](#); [Stellar feedback \(1602\)](#)

1. Introduction

Galactic scale outflows are prevalent in observations of star-forming galaxies (e.g., Veilleux et al. 2005; Rupke 2018, for reviews) and play a central role in contemporary theory of galaxy formation and evolution (e.g., Somerville & Davé 2015; Naab & Ostriker 2017, for reviews). Although single-phase outflows have often been adopted in cosmological subgrid models (e.g., Springel & Hernquist 2003; Oppenheimer & Davé 2006; Vogelsberger et al. 2013), real galactic outflows are clearly multiphase in nature (Veilleux et al. 2020, for a recent review). Multiwavelength observations of fast-moving gas include radio lines from cold molecular and atomic outflows (e.g., Leroy et al. 2015; Martini et al. 2018), optical and UV absorption lines from warm ionized outflows (e.g., Heckman et al. 2000, 2015; Martin 2005; Chisholm et al. 2016, 2017), and X-rays from hot ionized outflows (e.g., Lehnert et al. 1999; Strickland et al. 2004). Furthermore, numerical simulations that resolve the multiphase interstellar medium (ISM) in galaxies and include supernova (SN) feedback (e.g., Hopkins et al. 2012; Gatto et al. 2017; Li et al. 2017; Kim & Ostriker 2018; Hu 2019; Schneider et al. 2020) show that both warm/cold and hot gas in the ISM are driven out together by superbubble expansion and breakout. Thus, launching of multiphase outflows appears to be the generic outcome of SN feedback in star-forming galaxies.

In Kim et al. (2020, Paper I hereafter), we analyzed the outflows in a suite of parsec-resolution numerical simulations spanning a range of star-forming galaxy environments. We

separated out two distinct thermal phases at $T < 2 \times 10^4$ K (cool) and $T > 5 \times 10^5$ K (hot) with a subdominant intermediate phase at temperatures in between. For each phase, we characterized horizontally integrated mass, momentum, energy, and metal fluxes and loading factors (fluxes normalized by the corresponding star formation rate (SFR), or by the SN momentum, energy, and metal injection rate). We also measured horizontally averaged mean velocities of each outflow phase. In agreement with our previous study for solar neighborhood conditions (Kim & Ostriker 2018), Paper I showed that for all the environments investigated, (1) hot outflows deliver energy and SN-injected metals at high velocity to the circumgalactic medium (CGM), and (2) cool outflows carry much more mass, but at much lower velocity. We presented scaling relations for the dependence of multiphase outflow properties on the SFR, midplane pressure, and weight of the ISM, which are all (equally) good predictors for the mean outflow properties.

The characterization of Paper I addressed fundamental quantitative questions: how different are mass, momentum, energy, and metal outflow rates in different thermal phases? How do outflow rates scale with galactic conditions? However, in distilling “velocity-integrated” properties, important information regarding velocity and thermal distributions is lost. In particular, the cool-gas velocity distribution typically has an exponential wing extending to high velocity (Kim & Ostriker 2018; Vijayan et al. 2020), such that significant cool ISM material could escape into the CGM region even if the mean cool outflow velocity is lower than a galaxy’s escape speed.

Here we investigate the full joint probability density function (PDF) of outflow velocity and sound speed. We begin by showing that, given a mass loading PDF, the momentum, energy, and metal loading PDFs can be constructed (Section 2). We then develop a simple, parameterized model for the mass loading, with separate analytic functions describing cool and hot PDFs. These PDFs are combined with the scaling relations presented in Paper I to create an easy-to-use outflow launching model (Section 3), which can be implemented in either semi-analytic or fully numerical cosmological models of galaxy formation. We provide a Python package⁷ `Twind` for model PDFs and sampling, and demonstrate its application (Section 4 and Appendix B).

It should be borne in mind that the particular set of TIGRESS models we employ have several advantages, but also come with caveats, as discussed below. Thus, we consider the main goal of this Letter to be a proof of principle: we show that joint PDFs of outflow velocity and sound speed are an efficient yet accurate way to encapsulate complex outflow properties from multi-physics, high-resolution simulations. We further show that an analytic model representation of the joint PDFs enables immediate and practical application of the results from small scale simulations to cosmological simulations and semi-analytic models. While the demonstration employs our current TIGRESS simulation suite, results from other simulations (with additional physics and/or a wider parameter space) could be used in a similar fashion, fitting to obtain functional forms and parameters that characterize outflow PDFs based on kiloparsec-scale galactic properties.

2. Joint PDFs of Outflow Velocity and Sound Speed

We use a suite of local galactic disk models simulated with the TIGRESS framework (Kim & Ostriker 2017), as presented in Paper I. The suite comprises seven models, representing the range of galactic properties in nearby Milky Way-like star-forming galaxies, as summarized in Table 1. The self-regulated disk properties cover a wide range of SFR surface density ($\Sigma_{\text{SFR}} \sim 10^{-4}$ – $1 M_{\odot} \text{ kpc}^{-2} \text{ yr}^{-1}$), gas surface density ($\Sigma_{\text{gas}} \sim 1$ – $100 M_{\odot} \text{ pc}^{-2}$), and total midplane pressure/weight ($P_{\text{mid}}, \mathcal{W} \sim 10^3$ – $10^6 k_{\text{B}} \text{ cm}^{-3} \text{ K}$). We refer the reader to Paper I for full descriptions of models and methods (a brief summary can be found in Appendix A).

We note here that stellar feedback processes considered in the TIGRESS framework include grain photoelectric heating by far-UV (FUV) radiation (without explicit radiation transfer) and SNe from star clusters and runaway OB stars, while other feedback processes including radiation pressure, photoionization, stellar winds, and cosmic rays are neglected. The missing feedback processes may affect the total outflow rates and distributions directly, because some wind-driving forces such as cosmic-ray and ionized-gas pressure gradients (e.g., Emerick et al. 2018; Girichidis et al. 2018) are not represented, and/or indirectly, because early feedback might reduce clustering of star formation and SNe (e.g., Hopkins et al. 2020), which are known to enhance outflows (e.g., Fielding et al. 2018). We note that the effect of “early” feedback has explicitly been shown to be significant in dwarfs (Emerick et al. 2018; Smith et al. 2020), but is not yet fully demonstrated in Milky Way-like conditions as simulated in the TIGRESS suite. Also, the particular treatments in the TIGRESS framework for star formation using sink particles and

Table 1
Model Parameters

Model (1)	$\langle \Sigma_{\text{gas}} \rangle$ (2)	ρ_{sd} (3)	t_{orb} (4)	R_0 (5)	Δx (6)	$\langle \Sigma_{\text{SFR}} \rangle$ (7)
R2	74	1	61	2	2	1.1
R4	30	0.45	110	4	2	1.3×10^{-1}
R8	11	0.092	220	8	4	5.1×10^{-3}
R16	2.5	0.005	520	16	8	7.9×10^{-5}
LGR2	75	0.12	120	2	2	4.9×10^{-1}
LGR4	38	0.055	200	4	2	9.0×10^{-2}
LGR8	10	0.012	410	8	4	3.2×10^{-3}

Note. (1) Model name. (2) Gas surface density in $M_{\odot} \text{ pc}^{-2}$ averaged over $0.5 < t/t_{\text{orb}} < 1.5$. (3) Volume density of stars and dark matter at the midplane in $M_{\odot} \text{ pc}^{-3}$. (4) Orbit time $t_{\text{orb}} \equiv 2\pi/\Omega$ in Myr. (5) Galactocentric radius in kpc. (6) Spatial resolution of the simulation in pc. For all models, $(N_x, N_y, N_z) = (256, 256, 1792)$ grid zones are used. (7) SFR surface density in $M_{\odot} \text{ kpc}^{-2} \text{ yr}^{-1}$ averaged over $0.5 < t/t_{\text{orb}} < 1.5$.

SNe could potentially affect the properties of outflows (see Kim & Ostriker 2018 and Paper I for in-depth discussions). New metals (as opposed to the metals in the initial disk) in our simulations are injected only by SNe because we do not model stellar winds, which may affect the metallicity of outflows.

The above caveats and particularities certainly affect our specific quantitative results, but the overall approach we propose is quite general as a way to represent the mass, momentum, energy, and metals launched in multiphase outflows.

We now turn to distributions of outflowing gas in the TIGRESS suite. Let $f_q(u, w; z)$ be the PDF of an outflow quantity q at a given height z within logarithmic velocity bins of vertical outgoing velocity $u \equiv \log_{10} v_{\text{out}}$ and sound speed $w \equiv \log_{10} c_s$ in km/s:

$$f_q(u, w; z) \equiv \frac{1}{\langle q(z) \rangle} \frac{d^2 q(z)}{dudw}. \quad (1)$$

Here, f_q is in units of dex^{-2} , $q(z)$ is a quantity defined at height z over the entire x - y horizontal domain and the time interval $t \in (t_1, t_2)$ of interest, and $\langle q(z) \rangle$ is the temporal and horizontal average of q (also summed over all u and w) so that the time-averaged PDF has unit normalization, $\int f_q dudw = 1$. The physical quantities q of interest are vertical outgoing fluxes

$$\mathcal{F}_M = \rho v_{\text{out}} \quad (\text{mass flux}), \quad (2)$$

$$\mathcal{F}_p = \rho v_{\text{out}}^2 + P + \Pi_B \quad (z\text{-momentum flux}), \quad (3)$$

$$\mathcal{F}_E = \rho v_{\text{out}} v_B^2/2 + \mathcal{S}_z \quad (\text{energy flux}), \quad (4)$$

$$\mathcal{F}_Z = \rho Z v_{\text{out}} \quad (\text{metal flux}). \quad (5)$$

Here, $v_{\text{out}} \equiv v_z \text{sgn}(z)$ is the vertical outgoing velocity,

$$\Pi_B \equiv \frac{B^2}{8\pi} - \frac{B_z^2}{4\pi} \quad (6)$$

is the vertical component of the Maxwell stress (magnetic pressure + tension),

$$v_B \equiv \left(v^2 + \frac{2\gamma}{\gamma - 1} c_s^2 \right)^{1/2} \quad (7)$$

⁷ <https://twind.readthedocs.io>; all figures in this Letter are reproducible with the package.

is the Bernoulli velocity, where we use isothermal sound speed $c_s^2 \equiv P/\rho$, and

$$\mathcal{S}_z \equiv \frac{v_{\text{out}} B^2 - B_{\text{out}} \mathbf{v} \cdot \mathcal{B}}{4\pi} \quad (8)$$

is the vertical component of the Poynting flux with the vertical outgoing magnetic field $B_{\text{out}} = B_z \text{sgn}(z)$, and Z is metallicity as traced by passive scalars in the MHD simulations. Note that we adopt $\gamma = 5/3$ so that $2\gamma/(\gamma - 1) = 5$. In the outflow analysis of Paper I, we did not include magnetic terms in momentum and energy fluxes; Equations (3) and (4) include them for completeness but here we show they may be neglected.

The procedure to calculate the joint PDFs is as follows: we (1) extract one-zone thick slices at a distance from the midplane $|z|$ for both upper and lower sides (either fixed heights at $z = \pm 500$ pc and ± 1 kpc or time-varying heights at $z = \pm H$ and $\pm 2H$, where H is the instantaneous gas scale height) over $0.5 < t/t_{\text{orb}} < 1.5$, (2) sum up each quantity within square bins $du = dw = 0.02$ dex, and (3) normalize each PDF with the total ‘‘outflowing’’ quantity ($v_{\text{out}} > 0$) averaged over the time range of interest at a given height defined by

$$\langle q(z_k) \rangle \equiv \frac{\sum_{n,i,j} q(x_i, y_j, t_n; z_k) \Theta(v_{\text{out}} > 0)}{N_x N_y N_t}, \quad (9)$$

where $\Theta(C)$ is the top-hat-like filter that returns 1 if the conditional argument is true or 0 otherwise, N_x and N_y are the numbers of grid zones in the horizontal directions, and N_t is number of snapshots analyzed. In Paper I, we use $\bar{q}(z; t)$ to denote the horizontally integrated/averaged quantities that are outflowing with $v_{\text{out}} > 0$ (with a phase separation if needed) at a given time. Thus, $\langle q \rangle$ here is simply the time average of the corresponding \bar{q} , which is presented in Table 3 of Paper I and available online at doi:10.5281/zenodo.3872049.

In addition to the total metal flux, it is of interest to quantify how enriched the outflow is compared to the ISM. To derive the distribution of the outflow enrichment factor, we first define the average metallicity within each logarithmic velocity bin as

$$Z(u, w; z) \equiv \frac{\langle \mathcal{F}_Z(z) \rangle f_{\mathcal{F}_Z}(u, w; z)}{\langle \mathcal{F}_M(z) \rangle f_{\mathcal{F}_M}(u, w; z)} \quad (10)$$

so that the corresponding enrichment factor is

$$\zeta(u, w; z) \equiv \frac{Z(u, w; z)}{Z_{\text{ISM}}}. \quad (11)$$

The mean ISM metallicity Z_{ISM} is obtained by taking the time average of the instantaneous ISM metallicity $\bar{Z}_{\text{ISM}}(t)$ defined by the mean metallicity of the cool phase within $|z| < 50$ pc (see Section 4.2 of Paper I).

To make our approach more general, we translate our results into loading factors, defined by ratios of outflow fluxes to corresponding areal rates of star formation (and related areal rates) in our simulations. This translation eases the connection to global simulations, in which, e.g., the mass loading factor from a given cell represents the wind mass loss rate relative to SFR in that cell. We note that Σ_{SFR} is still needed for our model parameterization; in global models appropriate projection and averaging may be used to define Σ_{SFR} in the region centered on a given cell (of arbitrary shape).

Following Paper I, we define

$$\eta_q(x, y, t; z) = \frac{\mathcal{F}_q(x, y, t; z)}{\langle q_{\text{ref}} \Sigma_{\text{SFR}} / m_* \rangle}. \quad (12)$$

Here, $q = M, p, E$, and Z as in Equations (2)–(5), m_* is the mass of new stars formed per SN, and the reference values per SN event for mass, momentum, energy, and metal mass are

$$M_{\text{ref}} = m_* = 95.5 M_{\odot}, \quad (13)$$

$$p_{\text{ref}} = E_{\text{SN}} / (2v_{\text{cool}}) = 1.25 \times 10^5 M_{\odot} \text{ km s}^{-1}, \quad (14)$$

$$E_{\text{ref}} = E_{\text{SN}} = 10^{51} \text{ erg}, \quad (15)$$

$$Z_{\text{ref}} \equiv M_{\text{ej}} Z_{\text{SN}} = 2 M_{\odot}. \quad (16)$$

These values are adopted based on a Kroupa (2001) initial mass function, with ejecta mass $M_{\text{ej}} = 10 M_{\odot}$, and metallicity $Z_{\text{SN}} = 0.2$ from STARBURST99 (Leitherer et al. 1999). We choose $v_{\text{cool}} = 200$ km s^{−1} (see Section 4.1 of Paper I for the full discussion of this choice and p_{ref}). With these definitions, η_M is the ratio of mass outflow rate to SFR, η_E (η_Z) is the ratio of energy (metal mass) outflow rate to SN energy (SN metal mass) injection rate, and η_p is the ratio of z -momentum outflow rate to the vertical momentum injection rate from post-Sedov-stage SNe. Note that the PDFs are identical for fluxes and loading factors because they differ by a constant factor and are normalized to be integrated to 1. Therefore f_q with $q = M, p, E$, and Z may denote either a flux PDF or a loading PDF. We note also that loading factors may be defined for all material in the outflow or separated by thermal phase, depending on whether the corresponding flux is for all material or phase-separated (see Paper I).

Figure 1 shows⁸ (a) the mass loading PDF ($f_M(u, w)$), (b) the energy loading PDF ($f_E(u, w)$), and (c) the metal enrichment factor ($\zeta(u, w)$) for model R4 at $|z| = H$. As reported in Paper I (see also Kim & Ostriker 2018), it is evident that the cool outflow carries most of the mass (panel (a)), while the hot outflow carries most of the energy (panel (b)) and metals (panel (c)). In addition, Figure 1(b) clearly shows a wide distribution in v_{out} (with a narrow spread in c_s) for the cool outflow, contrasting in Figure 1(a) with a broader distribution along both axes for the hot outflow. This makes plain that naively adopting a single characteristic velocity and temperature would poorly represent both the mass and energy outflow rates.

For reference, Figure 1 includes contours of constant $v_{B,z}$, where the outflowing component of the Bernoulli velocity is defined as

$$v_{B,z} \equiv (v_{\text{out}}^2 + 5c_s^2)^{1/2}. \quad (17)$$

To gauge whether fluid elements with given (u, w) have sufficient energy to travel from the launching place to a distant location, $v_{B,z}$ can be compared to the escape velocity v_{esc} (which can be defined via the gravitational potential difference between wind launching position and the distant point).

For outflows driven under conditions like model R4 (with $\Sigma_{\text{SFR}} \sim 0.1 M_{\odot} \text{ kpc}^{-2} \text{ yr}^{-1}$), most hot outflows would escape the main galaxy if $v_{\text{esc}} \lesssim 300$ km s^{−1}, delivering significant energy and metal fluxes far into the CGM. Cool outflows in a massive galaxy, however, would fall back as fountains. In the case of a low-mass galaxy with a shallow halo potential, e.g.,

⁸ An equivalent figure for all seven models and four values of $|z|$ can be created using `Twind`. The same is true for all other figures.

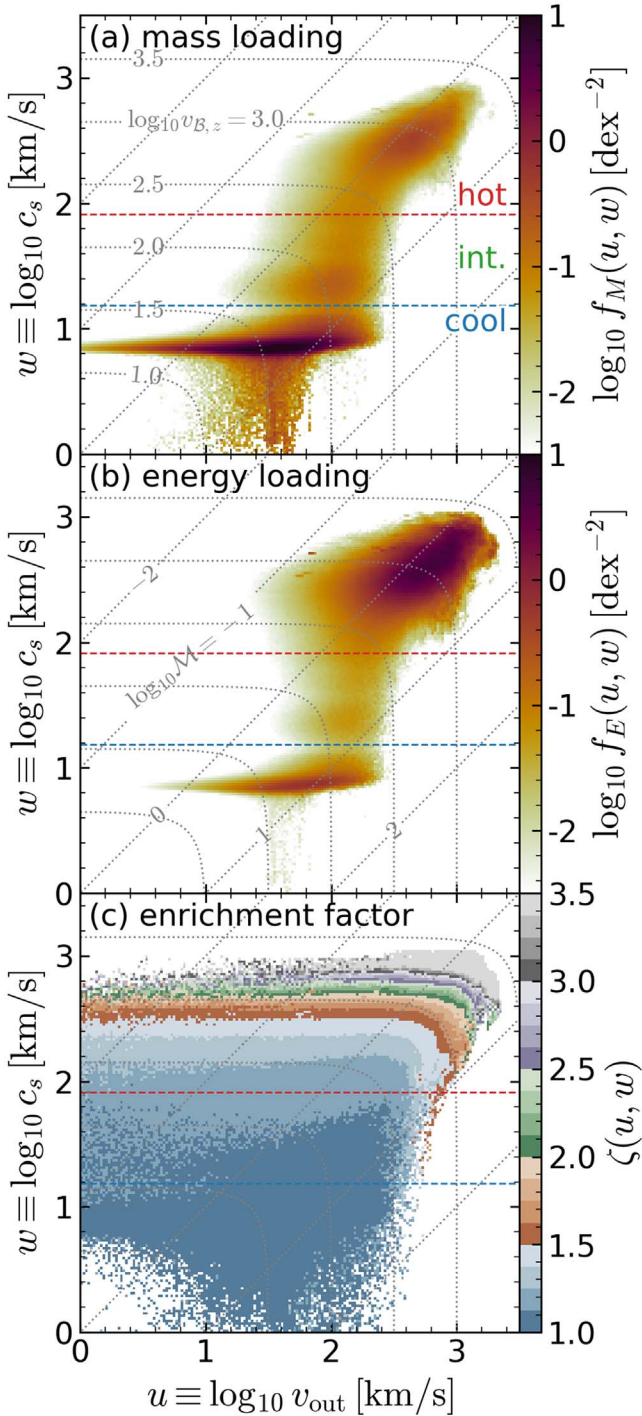


Figure 1. Joint PDFs in $\log_{10} v_{\text{out}}$ and $\log_{10} c_s$ for model R4 ($\Sigma_{\text{gas}} \sim 30 M_{\odot} \text{pc}^{-2}$ and $\Sigma_{\text{SFR}} \sim 10^{-1} M_{\odot} \text{kpc}^{-2} \text{yr}^{-1}$) at $|z| = H$. (a) Mass loading PDF, (b) energy loading PDF, and (c) enrichment factor distribution. The red and blue dashed lines denote temperature cuts to separate cool ($T < 2 \times 10^4 \text{K}$), intermediate ($2 \times 10^4 \text{K} < T < 5 \times 10^5 \text{K}$), and hot ($5 \times 10^5 \text{K} < T$) phases. The dotted gray lines denote loci of constant $v_{B,z} \equiv (v_{\text{out}}^2 + 5c_s^2)^{1/2}$ (labeled in (a)) and $M \equiv v_{\text{out}}/c_s$ (labeled in (b)); loci are identical in all panels.

$v_{\text{esc}} < 50 \text{ km s}^{-1}$, cool outflows would carry significant mass outside the main galaxy into the CGM, at the same time as the hot wind carries energy and momentum.

Figure 1(c) demonstrates that the enrichment factor is tightly related to $v_{B,z}$. This relation is rooted in the strong correlation between energy and SN-origin metal loading factors of the hot

outflow seen in Figure 15 of Paper I (see also Creasey et al. 2015; Li & Bryan 2020). We find that the model⁹

$$\tilde{\zeta} = \left(\frac{v_{B,z}}{3.2 \times 10^3 \text{ km s}^{-1}} \right)^{1.7} \left[\frac{Z_{\text{SN}}}{Z_{\text{ISM}}} - 1 \right] + 1 \quad (18)$$

for the enrichment factor defined in Equation (11) is in good agreement with the results for all heights ($|z| = H, 2H, 500 \text{ pc}$, and 1 kpc) where we measure the outflow properties from the full TIGRESS suite. As a result, for a given Z_{ISM} , model outflow metallicity $\tilde{Z} \equiv \tilde{\zeta} Z_{\text{ISM}}$ increases with the specific energy (or $v_{B,z}$) at high $v_{B,z}$ and flattens to Z_{ISM} at low $v_{B,z}$. This formula predicts that, even in the limit of zero ISM metallicity (although this is outside the parameter space we explored), the hot outflow at high v_B would have large non-zero metallicity $\tilde{Z} \propto Z_{\text{SN}} v_{B,z}^{1.7}$ derived from very recent SN ejecta. Note that Equation (18) uses $v_{B,z}$, which can be directly calculated from u and w . Paper I found a slight enrichment of the cool outflow ($\sim 10\%$ at the largest $\Sigma_{\text{SFR}} \sim 1 M_{\odot} \text{kpc}^{-2} \text{yr}^{-1}$), but we neglect it for simplicity. In Equation (18), $\tilde{\zeta} \rightarrow 1$ for low $v_{B,z}$, so the outflow metallicity model is valid for cool gas, in which \tilde{Z} approaches Z_{ISM} .

Under a certain set of assumptions, the momentum, energy, and metal loading PDFs can be recovered from the mass loading PDFs. If magnetic terms are negligible (and the bin size of PDFs is sufficiently small), the momentum loading PDF can be reconstructed from f_M as

$$f_p^r \equiv \frac{\langle \eta_M \rangle v_{\text{out}}^2 + c_s^2}{\langle \eta_p \rangle v_p v_{\text{out}}} f_M, \quad (19)$$

where $v_p \equiv p_{\text{ref}}/M_{\text{ref}} = 1.3 \times 10^3 \text{ km s}^{-1}$. The energy loading PDF can also be approximately reconstructed if the vertical component of kinetic energy dominates over the transverse component. In practice, there is a non-negligible contribution from the transverse component of kinetic energy, but we find we can correct for this. Our model results are consistent with a simple bias factor that describes the ratio of outflow component to total specific energy as a function of $v_{B,z}$:

$$b \equiv \frac{v_{B,z}^2}{v_B^2} = 0.1 \log_{10} v_{B,z} + 0.6, \quad (20)$$

for $v_{B,z}$ in units of km s^{-1} and $v_{B,z} \in (1, 10^4) \text{ km s}^{-1}$. We then obtain the reconstructed energy loading PDF from the mass loading PDF as

$$f_E^r \equiv \frac{\langle \eta_M \rangle}{\langle \eta_E \rangle} \frac{1}{2} \frac{v_{B,z}^2}{v_E^2} \frac{f_M}{b}, \quad (21)$$

where $v_E \equiv (E_{\text{ref}}/M_{\text{ref}})^{1/2} = 7.3 \times 10^2 \text{ km s}^{-1}$. Similarly, the metal loading PDF can be recovered using Equation (18) as

$$f_Z^r \equiv \frac{\langle \eta_M \rangle}{\langle \eta_Z \rangle} \frac{Z_{\text{ISM}} \tilde{\zeta}(v_{B,z})}{Z_e} f_M, \quad (22)$$

where $Z_e \equiv Z_{\text{ref}}/M_{\text{ref}} \rightarrow 0.02$.

To demonstrate how well PDFs for other variables can be recovered from the mass loading PDF with Equations (19),

⁹ Here and elsewhere we use a tilde to denote an analytic model, in which the parameters are determined by fits to the outputs of the TIGRESS simulation suite.

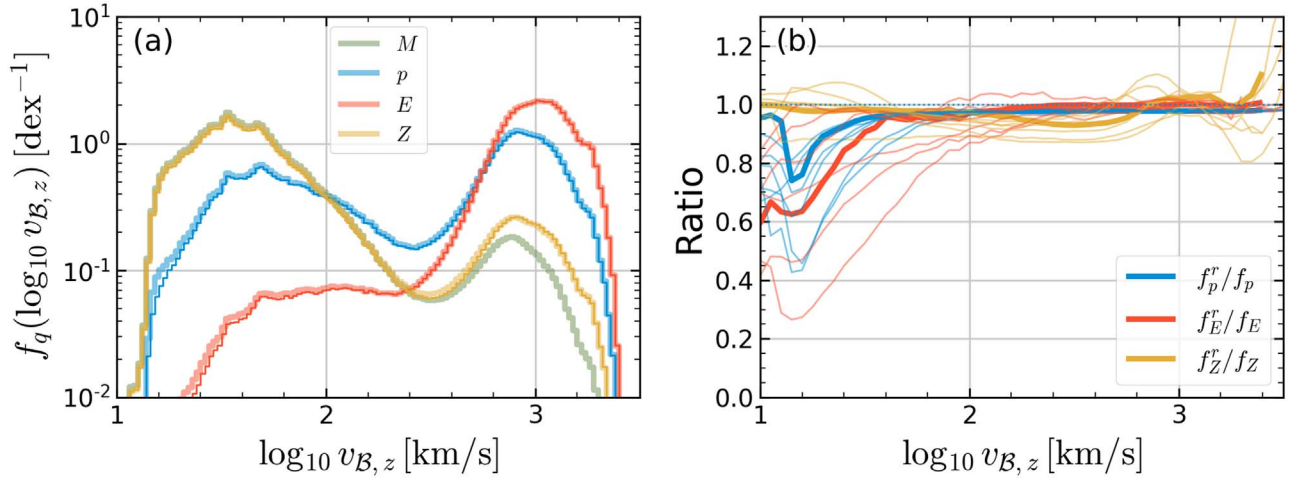


Figure 2. (a) Examples of PDFs for loading factors projected onto $\log_{10} v_{B,z}$ for model R4 at $|z| = H$. Thick lines show direct measurements of all PDFs, while thin lines with the same color (overlying the thick lines almost everywhere) show reconstructions from the mass PDF of momentum (Equation (19)), energy (Equation (21)), and metal (Equation (22)) PDFs. (b) The ratios of reconstructed PDFs to the original PDFs for all models at $|z| = H$. The mean ratio at a given $\log_{10} v_{B,z}$ is obtained from a mass-flux-weighted average. (Thick lines correspond to model R4, shown to the left.)

(21), and (22), Figure 2(a) plots the original PDFs projected onto the $\log_{10} v_{B,z}$ axis (thick lines), in comparison with the reconstructed PDFs (thin lines), for model R4 at $|z| = H$. The reconstruction is successful: the thin lines are barely seen as they overlie the thick lines almost everywhere. For more quantitative comparison, Figure 2(b) plots the ratios between reconstructed and original PDFs for all models at $|z| = H$ (thick lines are for R4 and thin lines for other models). Again, the recovery of all PDFs is quite good, especially at $v_{B,z}$ larger than a few tens of km s^{-1} (which is what matters in the outflow context). This justifies the general assumption that the magnetic stress is not important in outflows and confirms the validity of the enrichment factor model (Equation (18)) and the bias factor (Equation (20)) for all cases.¹⁰

3. Model PDFs and Validation

Figures 1 and 2 (see also Paper I) make clear that the cool gas and hot gas have quite different loading properties, which suggests that for practical applications it will be necessary to treat these components as two different *species*. To properly treat hot and cool winds on an individual basis, we first define an analytic two-component mass loading PDF model with an easy-to-use functional form that represents the results of the TIGRESS simulations well.¹¹ We then combine this with the scaling relations for phase-separated loading factors (presented in Table 5 of Paper I) and our reconstruction method (Equations (19), (21), and (22)) to derive energy, momentum, and metal loading PDFs. We emphasize that the objective is not to describe every detail of the PDFs but to reasonably capture the overall behavior over the range of $\Sigma_{\text{SFR}}/M_{\odot} \text{ kpc}^{-2} \text{ yr}^{-1} \in (10^{-4}, 1)$ covered in the simulation suite. With a goal of optimizing both physical fidelity and technical simplicity, we have found that just two free parameters are needed in our wind loading model: Σ_{SFR} and Z_{ISM} . As we shall show, these two parameters encapsulate the essential

aspects of local conditions of star-forming disks needed for characterizing wind properties.

For the cool outflow ($T < 2 \times 10^4 \text{ K}$), we find that a model combining log-normal and generalized gamma functions,

$$\tilde{f}_M^{\text{cool}}(u, w) = A_c \left(\frac{v_{\text{out}}}{v_{\text{out},0}} \right)^2 \exp \left[- \left(\frac{v_{\text{out}}}{v_{\text{out},0}} \right) \right] \times \exp \left[- \frac{1}{2} \left(\frac{\ln(c_s/c_{s,0})}{\sigma} \right)^2 \right], \quad (23)$$

describes the general shape of the distribution reasonably well. Here, $A_c = (\ln 10)^2 / (2\pi\sigma^2)^{1/2} = 2.12/\sigma$. For this functional form, the mean outflow velocity is $2v_{\text{out},0}$. To fit the simulation PDFs at $|z| = H$, we adopt constant values for $c_{s,0} = 6.7 \text{ km s}^{-1}$ and $\sigma = 0.1$, while $v_{\text{out},0}$ is a function of Σ_{SFR} :

$$v_{\text{out},0} = v_0 \Sigma_{\text{SFR},0}^{0.23} + 3 \text{ km s}^{-1} \quad (24)$$

where $v_0 = 25 \text{ km s}^{-1}$ and $\Sigma_{\text{SFR},0} \equiv \Sigma_{\text{SFR}}/M_{\odot} \text{ kpc}^{-2} \text{ yr}^{-1}$. The adopted form in Equation (24) differs slightly from the linear regression result presented in Paper I (Equation (57) there) to (1) adjust for a specific PDF shape adopted here, and (2) avoid arbitrarily low outflow velocity at very low Σ_{SFR} . We find that only small adjustments are needed in the parameters to describe the simulation PDFs at larger $|z|$: $(v_0, c_{s,0})/(\text{km s}^{-1}) = (45, 7.5)$, $(45, 8.5)$, and $(60, 10)$ at $|z| = 2H$, 500 pc, and 1 kpc, respectively. This adjustment is physically reasonable because only the higher $v_{B,z}$ components of cool outflows can travel farther.

For the hot outflow ($T > 5 \times 10^5 \text{ K}$), we construct a model mass PDF using two generalized gamma functions,

$$\tilde{f}_M^{\text{hot}}(u, w) = A_h \left(\frac{v_{B,z}}{v_{B,0}} \right)^2 \exp \left[- \left(\frac{v_{B,z}}{v_{B,0}} \right)^4 \right] \times \left(\frac{\mathcal{M}}{\mathcal{M}_0} \right)^3 \exp \left[- \left(\frac{\mathcal{M}}{\mathcal{M}_0} \right) \right]. \quad (25)$$

¹⁰ We also confirm that the same models can be applied to the results at all heights ($|z| = 2H$, 500 pc, and 1 kpc).

¹¹ For the purposes of quantifying winds, we do not separately analyze the coldest component ($T \lesssim 100 \text{ K}$), which may not be fully resolved in our simulations and does not contribute to mass, momentum, energy, and metal loading significantly.

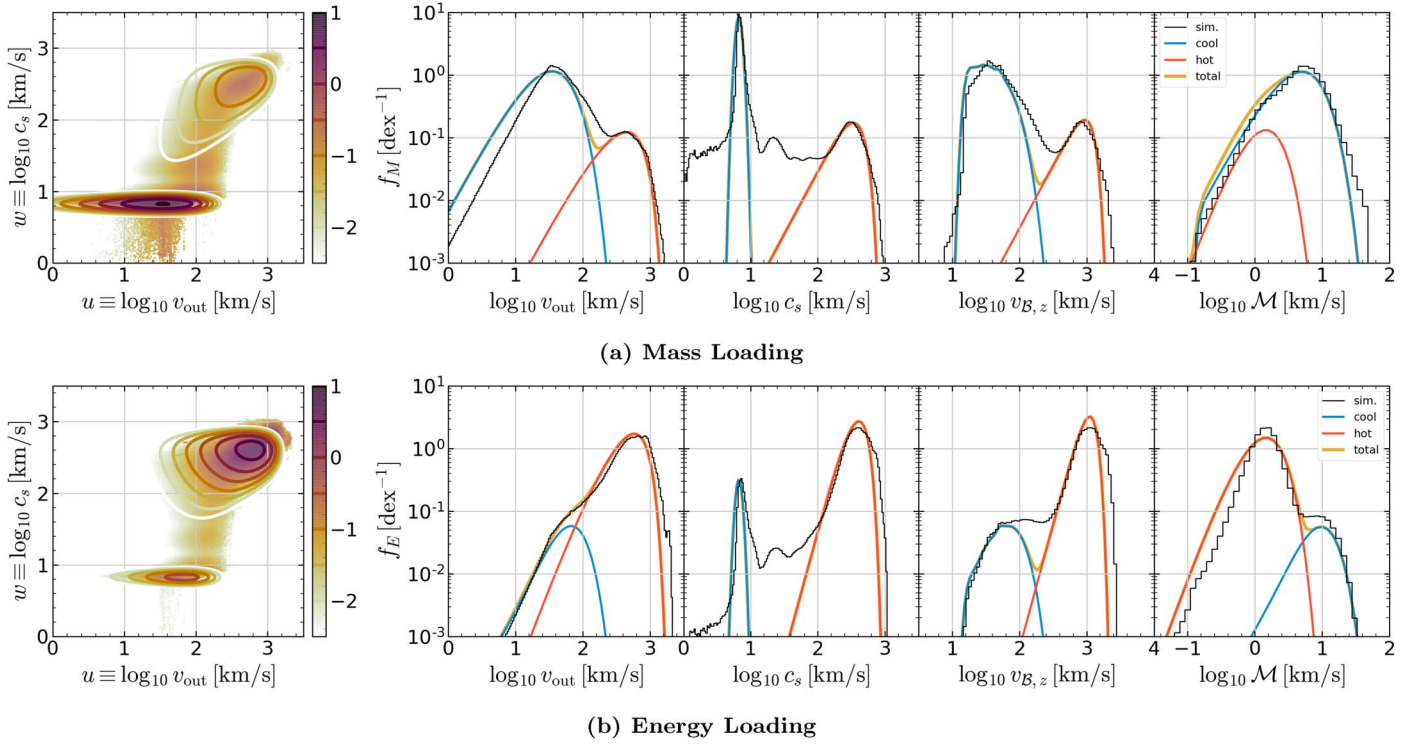


Figure 3. Comparison between simulated and model PDFs for R4 at $|z| = H$: (a) mass loading and (b) energy loading. In each row, the first column shows full joint PDFs on a logarithmic color scale ($\log_{10} f_{M,E}$ [dex^{-2}]) from the simulation (color) and model (contour). The remaining four panels are histograms showing projections onto (from left to right) v_{out} , c_s , $v_{B,z}$, and \mathcal{M} axes. Model PDFs are separated into cool (blue) and hot (orange) components. The sum of the two (yellow) matches simulated PDFs (black lines) well.

The arguments $v_{B,z} = (v_{\text{out}}^2 + 5c_s^2)^{1/2}$ and Mach number $\mathcal{M} \equiv v_{\text{out}}/c_s$ can be directly constructed from u and w . Here, $A_h = (\ln 10)^2 [2/\sqrt{\pi}] = 5.98$. For this functional form, the mean values of $v_{B,z}$ and \mathcal{M} are $0.69v_{B,0}$ and $3\mathcal{M}_0$. We adopt a constant value of $\mathcal{M}_0 = 0.5$, and a scaling relation for $v_{B,0}$:

$$\frac{v_{B,0}}{10^3 \text{ km s}^{-1}} = 2.4 \frac{\Sigma_{\text{SFR},0}^{1/2}}{2 + \Sigma_{\text{SFR},0}^{1/2}} + 0.8. \quad (26)$$

This adopted form is different from the linear regression presented in Paper I (Equation (60) there) to (1) keep $v_B \leq v_{\text{ej}}$ at high Σ_{SFR} and (2) accommodate a flattening at low Σ_{SFR} . The same hot outflow model works well at all four $|z|$ locations where the simulation PDFs are calculated. Given the generally high specific energy of the hot outflow, the shape of the PDF changes little within the range of $|z|$ we consider. Note that Equations (23) and (25) satisfy $\int \tilde{f}_M(u, w) du dw = 1$ individually.

As models for the mass loading of the cool and hot phases at $|z| = H$, we adopt power laws

$$\tilde{\eta}_M^{\text{cool}} = 0.85 \Sigma_{\text{SFR},0}^{-0.44} \quad (27)$$

$$\tilde{\eta}_M^{\text{hot}} = 0.20 \Sigma_{\text{SFR},0}^{-0.07} \quad (28)$$

similar to the relations derived in Paper I (see Figures 8(a), (b) there). As we are ignoring the intermediate component, the normalization in $\tilde{\eta}_M^{\text{hot}}$ is slightly larger (by a factor 1.4) than that in Paper I. We also note that $\tilde{\eta}_M \equiv \tilde{\eta}_M^{\text{cool}} + \tilde{\eta}_M^{\text{hot}}$ is not identical to the single combined power-law fit shown in Figure 13(a) of Paper I. The model mass PDF obtained by combining the cool

and hot components is given by

$$\tilde{f}_M(u, w) = \frac{\tilde{\eta}_M^{\text{cool}}}{\tilde{\eta}_M} \tilde{f}_M^{\text{cool}} + \frac{\tilde{\eta}_M^{\text{hot}}}{\tilde{\eta}_M} \tilde{f}_M^{\text{hot}}. \quad (29)$$

Figure 3 compares the simulated and model joint PDFs of model R4 in the (u, w) plane (first column, color and contour, respectively) and projections along the $\log_{10} v_{\text{out}}$, $\log_{10} c_s$, $\log_{10} v_{B,z}$, and $\log_{10} \mathcal{M}$ axes (from second column to fifth). Panels with projected PDFs show the combined model (yellow lines) and the individual cool (blue lines) and hot (red lines) components separately. The combined model PDF follows the original PDF from the simulation (shown as black) reasonably well, modulo a dearth of intermediate-temperature gas $w \in (1, 2)$ and cold gas $w < 0.5$ (but since these have low mass *and* energy loading factors, this makes no practical difference).

We derive model PDFs for momentum, energy, and metal loading factors as

$$\tilde{f}_q = \frac{\tilde{\eta}_q^{\text{cool}}}{\tilde{\eta}_q} \tilde{f}_q^{\text{cool},r} + \frac{\tilde{\eta}_q^{\text{hot}}}{\tilde{\eta}_q} \tilde{f}_q^{\text{hot},r} \quad (30)$$

where $q = p, E$, and Z , and $\tilde{f}_q^{\text{ph},r}$ is the reconstructed model PDF for each phase (ph = cool or hot) using Equations (19), (21), and (22). As an example, for momentum

$$\tilde{f}_p^{\text{ph},r} = \frac{\tilde{\eta}_M^{\text{ph}} v_{\text{out}}^2 + c_s^2}{\tilde{\eta}_p^{\text{ph}} v_p v_{\text{out}}} \tilde{f}_M^{\text{ph}}, \quad (31)$$

with analogous expressions for $\tilde{f}_E^{\text{ph},r}$ and $\tilde{f}_Z^{\text{ph},r}$ based on Equations (21) and (22). As we combine Equations (30) and (31)

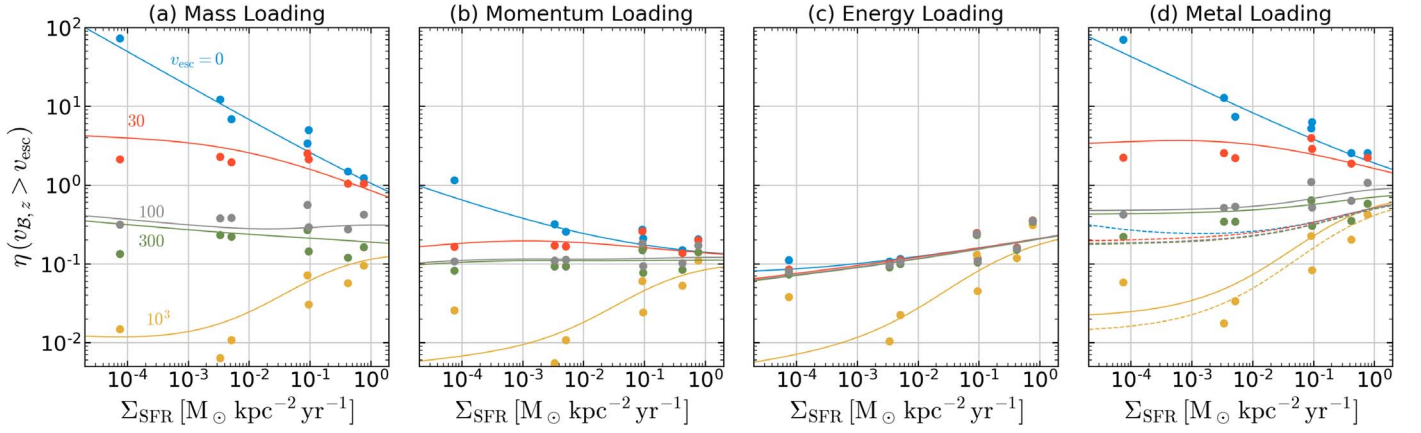


Figure 4. Loading factors for outflows with $v_{B,z} > v_{esc}$ (Equation (35)) at $|z| = H$. Filled circles are directly calculated from the simulation PDFs, while solid lines are from the model PDFs. Solid and dashed lines in (d) denote the model loading factors for $Z_{ISM} = 0.02$ and 0, respectively. Overall, the model tracks the general behavior of the simulation results.

(or analogous expressions for $q = E$ and Z), $\tilde{\eta}_q^{\text{ph}}$ cancels out, and we only need models for the *total* momentum, energy, and metal loading factors once we have constructed \tilde{f}_M using the phase-separated $\tilde{\eta}_M^{\text{cool}}$ and $\tilde{\eta}_M^{\text{hot}}$. We combine the power laws in Σ_{SFR} for cool and hot phases at $|z| = H$ from Table 5 of Paper I¹² to obtain total loading factors:

$$\tilde{\eta}_p = 0.04 \Sigma_{\text{SFR},0}^{-0.29} + 0.1 \Sigma_{\text{SFR},0}^{0.02} \quad (32)$$

$$\tilde{\eta}_E = 0.01 \Sigma_{\text{SFR},0}^{-0.12} + 0.2 \Sigma_{\text{SFR},0}^{0.14} \quad (33)$$

$$\tilde{\eta}_Z = 1.5 \Sigma_{\text{SFR},0}^{-0.36} + 0.42 \Sigma_{\text{SFR},0}^{0.04} \quad (34)$$

We then renormalize the reconstructed model PDFs to make $\int \tilde{f}_q dudw = 1$.

Figure 3(b) shows the model energy loading PDF \tilde{f}_E in comparison to the simulated energy loading PDF. Again, the agreement between the simulated and model PDFs is good.

To check the validity of the model PDFs over a range of Σ_{SFR} , we compute loading factors for outflows for $v_{B,z} > v_{esc}$,

$$\eta_q(v_{B,z} > v_{esc}) \equiv \tilde{\eta}_q \int_{v_{B,z}=v_{esc}}^{\infty} \tilde{f}_q(u, w) dudw, \quad (35)$$

where $q = M, p, E,$ and Z . Figure 4 compares the model $\eta_q(v_{B,z} > v_{esc})$ at varying $v_{esc} = 0, 30, 100, 300,$ and 10^3 km s^{-1} to direct results from the simulations at $|z| = H$. These can be thought of as idealized outflow loading properties in halos with varying escape velocities. Direct results from the TIGRESS simulations are shown as filled circles, and the model compares well at all Σ_{SFR} and v_{esc} .

Note that for the purpose of this test, we normalize the model metal loading PDF for a fixed ISM metallicity, $Z_{ISM} = 0.02$. We plot as dashed lines in panel (d) the results for $Z_{ISM} = 0$, which are equivalent to the instantaneous SN-origin metal loading factors. This puts a floor on the metal loading.

Despite its simplicity, the model correctly captures key behaviors from the simulations remarkably well. In particular, the high sensitivity of mass loading to v_{esc} (most extreme at low Σ_{SFR}) and the general insensitivity of energy loading to v_{esc} and Σ_{SFR} are notable. The former effect is due to the increase in the

mass loading and the decrease in outflow velocities of cool gas at low Σ_{SFR} , while the latter effect is a result of the high outflow velocity and near-constant energy loading of hot gas produced by SNe. More subtle effects, such as the moderate decrease in energy loading at low Σ_{SFR} when $v_{esc} > 300 \text{ km s}^{-1}$, are also reproduced by the model. We note that the energy loading behavior of the model is mirrored in the metal loading for $Z_{ISM} = 0$ because this is from SN ejecta, while the increase in metal loading at low v_{esc} for $Z_{ISM} = 0.02$ is due to metal loss in low-velocity cool ISM gas.

4. Practical Application

For practical implementation of our wind launching model, we release a Python package *Twind* with our wind model. As cosmological simulations often launch winds as particles (e.g., Oppenheimer & Davé 2006; Vogelsberger et al. 2013; but see Dubois & Teyssier 2008; Dalla Vecchia & Schaye 2012; Keller et al. 2014 for alternative approaches), the package also implements a particle sampling procedure. *Twind* is based on the two-component PDF model at $|z| = H$ described in Section 3, but also supports models at different heights $|z| = 2H, 500 \text{ pc},$ and 1 kpc .

We demonstrate *Twind* following the procedure outlined in Appendix B using the R8 TIGRESS model, which has the longest simulation duration in our simulation suite. We treat our whole simulation box as equivalent to one resolution element in a cosmological simulation, giving a time series $\dot{M}_* = \Sigma_{\text{SFR}} L_x L_y$ where $L_x L_y = (1024 \text{ pc})^2$ is the horizontal area of the simulation. For this demonstration, we fix $\Delta t = 1 \text{ Myr}$, and adopt constant mass quanta m^{cool} and m^{hot} .

Figure 5 shows (a) the mass outflow rate of cool gas from the simulation (black) and the model with three different m^{cool} ; (b) the energy outflow rate of hot gas from the simulation (black) and the model with three different m^{hot} ; and (c) the distribution of hot (squares) and cool (circles) particles for the different choices of particle masses. For simplicity, we only show mass (energy) outflow rates of the dominating cool (hot) component (see Figure 3).

As the adopted SFR varies with time, the target mass outflow rate also fluctuates, with median $3.7 \times 10^{-2} M_{\odot} \text{ yr}^{-1}$ and 5th (95th) percentile 9.6×10^{-3} (6.4×10^{-2}) $M_{\odot} \text{ yr}^{-1}$. For our chosen $\Delta t = 1 \text{ Myr}$, this translates into outflow mass $\sim 10^4$ – $10^5 M_{\odot}$, mostly in cool gas. We thus expect complete,

¹² In order to construct model PDFs at different $|z|$, one should adjust the scaling relations of the loading factors to those from the given height, which are available at doi:10.5281/zenodo.3872049.

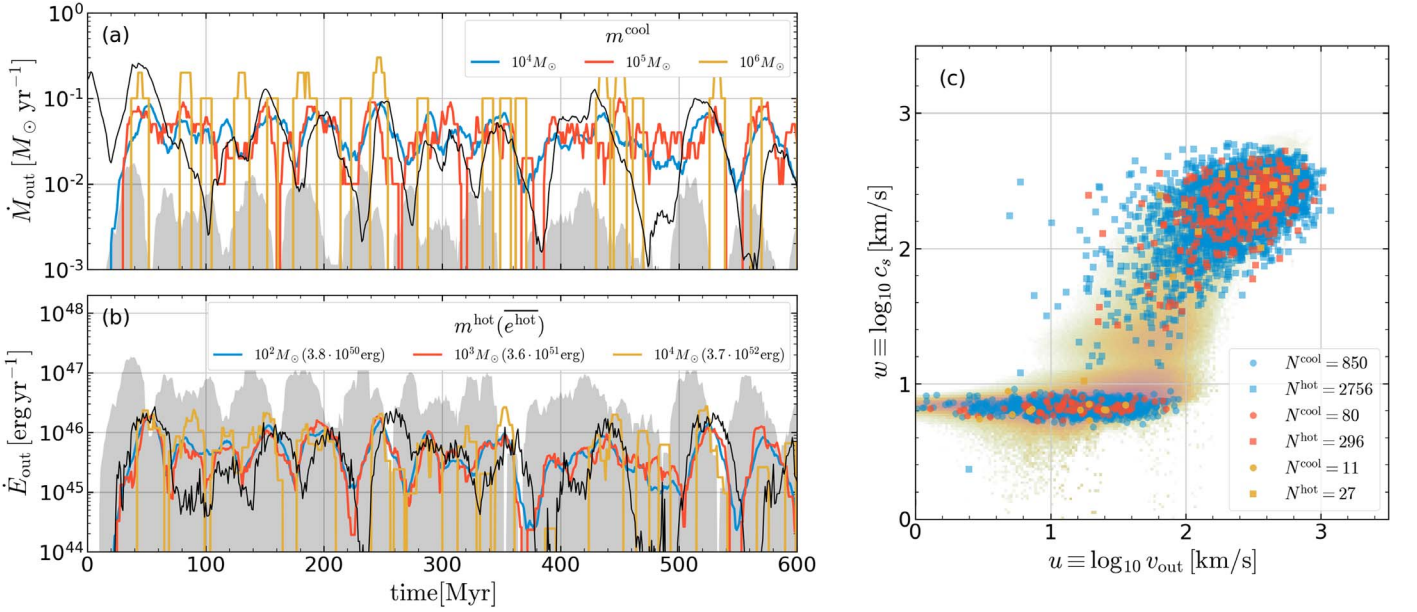


Figure 5. Demonstration of model sampling for (a) mass outflow rate of cool gas and (b) energy outflow rate of hot gas at $|z| = H$. The simulation result (black solid) is compared to the model for three different choices of particle mass (colored lines; see keys). The input to the model is $\Sigma_{\text{SFR}}(t)$ from TIGRESS simulation R8 (representing solar neighborhood conditions with $\Sigma_{\text{gas}} \sim 10 M_{\odot} \text{pc}^{-2}$ and $\Sigma_{\text{SFR}} \sim 5 \times 10^{-3} M_{\odot} \text{kpc}^{-2} \text{yr}^{-1}$), where $\dot{M}_{*} = \Sigma_{\text{SFR}} L_{*} L_{y}$ is shown as the gray shaded region in (a) and the corresponding SN energy injection rate is shown as the gray region in (b). (c) Distributions of cool (circles) and hot (squares) outflow particles sampled over $t = 220\text{--}440$ Myr from the different mass sampling cases (number of particles drawn is shown in the legend). The simulation PDF at $|z| = H$ over the same time interval is shown in the background.

marginal, and incomplete sampling of cool outflows for $m^{\text{cool}} = 10^4 M_{\odot}$, $10^5 M_{\odot}$, and $10^6 M_{\odot}$, respectively. Figure 5(a) is consistent with this expectation, with good temporal tracking at the lower two masses and poor tracking at the highest mass.¹³

For the R8 simulation, the 5th and 95th percentiles of the energy outflow rate are 4.9×10^{44} and $1.4 \times 10^{46} \text{ erg yr}^{-1}$, corresponding to a range $\sim 5 \times 10^{50}\text{--}10^{52} \text{ erg}$ for $\Delta t = 1$ Myr. Given the mass of hot particles and the model PDF, the mean particle energy is $e^{\text{hot}} \sim 4 \times 10^{50} \text{ erg}$ for $m^{\text{hot}} = 10^2 M_{\odot}$ and increases nearly linearly with the particle mass. Therefore, we expect complete, marginal, and incomplete sampling of hot outflows for $m^{\text{hot}} = 10^2 M_{\odot}$, $10^3 M_{\odot}$, and $10^4 M_{\odot}$, respectively, as Figure 5(b) demonstrates.

More generally, the necessary resolutions for a fair sampling of mass and energy outflow rates by cool and hot gas, respectively, are

$$m^{\text{cool}} \sim \eta_M^{\text{cool}} \dot{M}_{*} \Delta t \quad (36)$$

$$\frac{\overline{v_{B,z}}^2}{2} m^{\text{hot}} \sim \eta_E^{\text{hot}} E_{\text{SN}} \frac{\dot{M}_{*}}{m_{*}} \Delta t, \quad (37)$$

where $\overline{v_{B,z}} = 0.69 v_{B,0}$ is the mean Bernoulli velocity of the hot PDF (Equation (25)). This implies that the ratio of resolution for hot and cool gas particles should obey

$$\frac{m^{\text{hot}}}{m^{\text{cool}}} \approx \frac{4E_{\text{SN}}}{m_{*} v_{B,0}^2} \frac{\eta_E^{\text{hot}}}{\eta_M^{\text{cool}}}, \quad (38)$$

which is $\sim 0.01\text{--}0.1$ in our simulations (increasing with Σ_{SFR}). In simulations using particle-based codes, the hot wind

particles would therefore generally need to be spawned with smaller mass than the common mass resolution of gas particles.

5. Summary and Outlook

Outflows produced by SN feedback include both hot and cool phases, and even within a single phase there is a range of temperature and flow velocity. Here, we extend the analysis of Paper I using joint PDFs in sound speed and outflow speed to characterize the mass, momentum, energy, and metal loading of the outflowing gas in a TIGRESS simulation suite, treating cool and hot components separately. We demonstrate that the mass loading PDFs are well described by straightforward analytic expressions (Equations (23) and (25)). The momentum, energy, and metal loading PDFs can then be reconstructed from the mass loading PDFs without significant loss of information. A sampling procedure utilizing our two-component PDF, prototyped in Python as `Twind`, is able to successfully reproduce the time-dependent simulated outflow rates in TIGRESS, provided that the respective mass and energy samplings of cool- and hot-phase outflows are sufficient to follow the true temporal evolution.

The framework developed in this Letter for characterizing multiphase outflows using joint PDFs is quite general, and can be applied to any existing and future simulations in which multiphase outflows naturally emerge. Additional feedback processes including cosmic rays, stellar winds, and radiation as well as additional physics (e.g., thermal conduction) or global geometry may alter the parameters compared to those calibrated using our existing TIGRESS simulation suite. Different functional forms might be needed as well. Regardless of particular details, we consider the formalism we have introduced to analyze simulations and characterize joint PDFs of outflow velocity and sound speed as a fundamental advance in the representation of multiphase outflows.

¹³ In both panels, model outflow rates are shifted by 10 Myr since there is a time delay between star formation/SN events near the midplane and gas outflows passing through one scale height above the midplane (see Appendix C in Paper I).

The joint PDF model and sampling procedure outlined here can be applied to launch multiphase wind particles in cosmological simulations. This would require several changes with respect to current practices in big-box cosmological simulations. First, it is crucial to separately model hot and cool components, rather than a single component. Second, the two components should have separate mass resolution, since resolving energy outflows in the hot gas requires a hot-gas particle mass one or two orders of magnitude lower than the particle mass required to resolve cool outflows.

In particular, we consider sampling requirements for a solar neighborhood environment with $\Sigma_{\text{SFR}} \sim 3 \times 10^{-3} M_{\odot} \text{ kpc}^{-2} \text{ yr}^{-1}$, which is typical of star-forming disks in both observations (e.g., Sun et al. 2020) and simulations (e.g., Motwani et al. 2020). The mass resolution for baryons adopted in the Illustris-TNG50 simulations (Nelson et al. 2019; Pillepich et al. 2019) is $\sim 10^5 M_{\odot}$, which would be marginal for realizing mass outflow in cool gas but insufficient for realizing energy (and metal) delivery in hot outflows.

The wind launching model outlined here requires just two parameters, the local ISM metallicity Z_{ISM} and the local SFR per unit area in the disk, Σ_{SFR} . The first is readily available in current cosmological simulation frameworks, but the latter typically is not. There are two different issues. First, the disk scale height is generally not resolved in the current generation of large-volume simulations. As a result, the true volume density (or pressure) of gas is not known, and without knowledge of the corresponding internal dynamical timescales it is not possible to make a physically based prediction for the SFR on a cell-by-cell basis. To address this issue, either the scale height must be resolved (e.g., in zoom simulations) or a subgrid model for estimating the true gas scale height must be included. Second, to obtain Σ_{SFR} on-the-fly for individual cells, additional computation involving some overhead (e.g., for neighbor searches) would be required.

While the new approach to subgrid wind modeling we describe would involve technical challenges and computational costs, the return on the investment would be wind properties that represent local environments much more faithfully than current approaches. In particular, the usual practice in current cosmological simulations is to scale wind velocities relative to halo virial velocity (e.g., Davé et al. 2016, 2019; Pillepich et al. 2018), but this does not properly represent the physics of cool gas acceleration, which mostly takes place at small scales within or near the disk in response to the *local* rate of SN explosions. A wind launching model calibrated based on resolved local simulations would also be predictive and testable through, e.g., global correlations of galaxy properties, which is not the case for empirically tuned subgrid models.

The results presented here are also of immediate practical use in semi-analytic models (SAMs) of galaxy formation (e.g., Somerville et al. 2015; Forbes et al. 2019). In contrast to traditional approaches adopted in SAMs, the inclusion of both mass and energy loading factors enables more sophisticated modeling. For example, many SAMs only account for the mass loss from the ISM due to outflows, and do not include the effects of energy deposited by winds. Pandya et al. (2020) have shown that preventative feedback due to energy deposition from stellar feedback-driven winds may be needed to allow SAMs to better reproduce the predictions from the FIRE-2 numerical hydrodynamic simulation suite (Hopkins et al. 2018), especially in dwarf galaxies. Furthermore, a primary uncertainty in SAMs is

what fraction of gas ejected by stellar feedback-driven winds escapes the halo, and on what timescale this ejected gas returns to the halo. The v_{esc} -dependent loading factors presented here can be used to determine these quantities, thereby removing several of the free parameters that needed to be empirically calibrated in previous generations of SAMs.

Finally, we emphasize that our model only provides outflow properties at launching, close to the galactic disk ($|z| < 1 \text{ kpc}$). To understand and model the impact of multiphase outflows in the context of galaxy formation and evolution, it is necessary to follow *wind interactions* with the CGM (which may be inflowing; e.g., Melso et al. 2019; Gurvich et al. 2020). These may or may not be resolved in cosmological simulations, or explicitly modeled in SAMs. It is known from zoom-in simulations that there can be large differences between loading factors near the disk and after the interaction with the CGM (e.g., Muratov et al. 2015; Anglés-Alcázar et al. 2017; Tollet et al. 2019), which implies that additional “post-launch” subgrid treatments would be required for lower-resolution large-box simulations. Efforts are underway within the SMAUG collaboration to implement our *wind launching* model, together with additional treatments for the interaction with the CGM, both in numerical hydrodynamic simulations and in next-generation SAMs.

This work was carried out as part of the SMAUG project. SMAUG gratefully acknowledges support from the Center for Computational Astrophysics at the Flatiron Institute, which is supported by the Simons Foundation. We appreciate the constructive report from the referee. We are grateful to Ulrich Steinwandel, Viraj Pandya, Miao Li, and the rest of the SMAUG members for valuable discussions and helpful comments on the manuscript. The work of C.-G.K. was supported in part by a grant from the Simons Foundation (CCA 528307, E.C.O.). C.-G.K. and E.C.O. were supported in part by NASA ATP grant No. NNX17AG26G. The work of M.C.S. was supported by a grant from the Simons Foundation (CCA 668771, L.E.H.). G.L.B. acknowledges financial support from the NSF (grant AST-1615955, OAC-1835509). Resources supporting this work were provided in part by the NASA High-End Computing (HEC) Program through the NASA Advanced Supercomputing (NAS) Division at Ames Research Center, in part by the Princeton Institute for Computational Science and Engineering (PICSciE) and the Office of Information Technology’s High Performance Computing Center, and in part by the National Energy Research Scientific Computing Center, which is supported by the Office of Science of the U.S. Department of Energy under Contract No. DE-AC02-05CH11231.

Software: Athena (Stone et al. 2008; Stone & Gardiner 2009), astropy (Astropy Collaboration et al. 2013, 2018), scipy (Virtanen et al. 2020), numpy (Harris et al. 2020), IPython (Perez & Granger 2007), matplotlib (Hunter 2007), xarray (Hoyer & Hamman 2017), pandas (McKinney 2010), CMasher (van der Velden 2020), adstex (<https://github.com/yymao/adstex>).

Appendix A

A Brief Summary of Models and Methods

The TIGRESS framework solves the ideal MHD equations on a uniform Cartesian grid using Athena (Stone et al. 2008; Stone & Gardiner 2009). We use a standard local shearing box in which $x = R - R_0$ and $y = R(\phi - \Omega t)$ are the local Cartesian coordinates at galactocentric distance R_0 (with box center rotating

at angular speed Ω about the galactic center), while z is the global vertical coordinate centered at the disk midplane. The energy equation includes a net cooling term, $\mathcal{L} = n_{\text{H}}^2 \Lambda(T) - n_{\text{H}} \Gamma$, where n_{H} is the hydrogen number density, $\Lambda(T)$ is the temperature-dependent cooling coefficient at solar metallicity adopted from Koyama & Inutsuka (2002) at $T < 10^{4.2}$ K and from Sutherland & Dopita (1993) at $T > 10^{4.2}$ K, and Γ is the FUV-dependent heating rate due to the photoelectric effect on small grains, allowing for plane-parallel attenuation of FUV radiation. The Poisson equation is solved to obtain the gravitational potential from gas and newly formed star clusters. Self-gravitating collapse is followed up to the density threshold ($> 10^2\text{--}10^3 \text{ cm}^{-3}$, higher in models with higher surface density); above this density sink particles may be created to represent star clusters if flows are converging in all three directions and there is a local minimum of the gravitational potential. A simple stellar population synthesis model from STARBURST99 (Leitherer et al. 1999) is used to obtain the FUV luminosity and SN rate of each cluster particle. SN events are modeled by either energy injection or momentum injection depending on the resolution and the density of the surrounding medium (Kim & Ostriker 2015). Our resolution is high enough to resolve the Sedov–Taylor stage of almost all SNe ($> 90\%$), which is critical for multiphase outflow driving.

We note that our treatments of sink particles and SNe from them may enhance clustering of SNe, and the resulting “burstiness” may affect outflow properties. We convert all the gas in cells experiencing unresolved gravitational collapse into sink particles (assuming 100% star formation efficiency within gravitationally collapsing cores). Each particle represents a star cluster with mass of M_{cl} . Typical cluster masses are in the range of $10^3\text{--}10^5 M_{\odot}$, while a few $\sim 10^6 M_{\odot}$ clusters also form in the models with high gas surface density, R2 and LGR2. Each cluster particle creates $N_{\text{SN}} \sim M_{\text{cl}}/m_{*} = 10(M_{\text{cl}}/10^3 M_{\odot})$ core-collapse SNe over ~ 40 Myr. Two-thirds of them explode at the position of the hosting cluster particle, while one-third are treated as OB runaways ejected from the hosting cluster at high velocity before explosion.

We use the standard model suite presented in Paper I. The suite consists of seven models, with key parameters summarized in Table 1.

Appendix B Twind Sampling Procedure

Given a total SFR \dot{M}_{*} , and wind mass quantum m^{ph} in each phase ($\text{ph} \in \{\text{cool}, \text{hot}\}$), the sampling procedure is as follows.

1. Obtain the mass of the wind for each phase:

$$M_{\text{wind}}^{\text{ph}} = \tilde{\eta}_M^{\text{ph}} \dot{M}_{*} \Delta t, \quad (\text{B1})$$

where Δt is the time interval (which can be a simulation time step).

2. Draw an integer random variate N^{ph} from the Poisson distribution to choose the number of wind particles to spawn:

$$N^{\text{ph}} \sim \text{Pois}(k; \lambda), \quad (\text{B2})$$

where $\text{Pois}(k; \lambda) = \lambda^k e^{-\lambda}/k!$ is the Poisson distribution with the Poissonian mean $\lambda \equiv M_{\text{wind}}^{\text{ph}}/m^{\text{ph}}$.

3. Draw two random numbers ξ_1 and ξ_2 for each particle to assign v_{out} and c_s . ξ_1 and ξ_2 are drawn either from a two-parameter generalized Gaussian distribution (GGD; $G(x; d, p)$) and standard normal distribution ($g(x)$) for cool particles, or from two two-parameter GGDs

for hot particles:

$$\xi_1 \sim G(x; 2, 1), \quad \xi_2 \sim g(x) \quad \text{if ph} = \text{cool} \quad (\text{B3})$$

$$\xi_1 \sim G(x; 2, 4), \quad \xi_2 \sim G(x; 3, 1) \quad \text{if ph} = \text{hot}, \quad (\text{B4})$$

where $G(x; d, p) \equiv x^{d-1} e^{-x^p} p / \Gamma(d/p)$ is the two-parameter GGD and $g(x) \equiv \exp(-x^2/2)/(2\pi)^{1/2}$ is the standard normal distribution. In practice, we tabulate the inverse of the cumulative distribution function (CDF) of three GGDs with parameters used in Equations (B3) and (B4) and obtain $\xi_i = \text{CDF}^{-1}(\xi_{U,i})$, where $\xi_{U,i}$ is a uniform random number in $[0, 1)$.

4. Assign v_{out} and c_s : if $\text{ph} = \text{cool}$,

$$v_{\text{out}} = v_{\text{out},0} \xi_1, \quad c_s = c_{s,0} e^{\xi_2 \sigma}; \quad (\text{B5})$$

and if $\text{ph} = \text{hot}$,

$$c_s = v_{B,z} / (\mathcal{M}^2 + 5)^{1/2}, \quad v_{\text{out}} = \mathcal{M} c_s, \quad (\text{B6})$$

$$\text{where } v_{B,z} = v_{B,0} \xi_1, \quad \mathcal{M} = \mathcal{M}_0 \xi_2. \quad (\text{B7})$$

Here, $c_{s,0}$, σ , and \mathcal{M}_0 are constants while $v_{\text{out},0}$ and $v_{B,0}$ are functions of Σ_{SFR} (see Section 3). To fit the simulation PDFs at different heights ($|z| = H, 2H, 500 \text{ pc}, 1 \text{ kpc}$), we adjust these parameters and change $\tilde{\eta}_q$ from Paper I. These explicit parameterizations are implemented in `Twind`.

5. Assign metals to the particle based on the metallicity in the launching region (Z_{ISM}) and the metal enrichment factor (Equation (18)).
6. (Optional) Assign the velocity perpendicular to the outflow direction to the particle based on Equation (20):

$$v_{\perp} = \left(\frac{1-b}{b} \right)^{1/2} v_{B,z}. \quad (\text{B8})$$

In Section 4, we draw samples with a fixed particle mass because this is the typical practice in cosmological simulations, but it is also straightforward to draw samples for a fixed particle energy.


ORCID iDs

Chang-Goo Kim  <https://orcid.org/0000-0003-2896-3725>

Eve C. Ostriker  <https://orcid.org/0000-0002-0509-9113>

Drummond B. Fielding  <https://orcid.org/0000-0003-3806-8548>

Matthew C. Smith  <https://orcid.org/0000-0002-9849-877X>

Greg L. Bryan  <https://orcid.org/0000-0003-2630-9228>

Rachel S. Somerville  <https://orcid.org/0000-0003-2835-8533>

John C. Forbes  <https://orcid.org/0000-0002-1975-4449>

Shy Genel  <https://orcid.org/0000-0002-3185-1540>

Lars Hernquist  <https://orcid.org/0000-0001-6950-1629>

References

- Anglés-Alcázar, D., Faucher-Giguère, C.-A., Kereš, D., et al. 2017, *MNRAS*, **470**, 4698
- Astropy Collaboration, Price-Whelan, A. M., Sipőcz, B. M., et al. 2018, *AJ*, **156**, 123
- Astropy Collaboration, Robitaille, T. P., Tollerud, E. J., et al. 2013, *A&A*, **558**, A33
- Chisholm, J., Tremonti, C. A., Leitherer, C., & Chen, Y. 2017, *MNRAS*, **469**, 4831

- Chisholm, J., Tremonti, C. A., Leitherer, C., Chen, Y., & Wofford, A. 2016, *MNRAS*, **457**, 3133
- Creasey, P., Scannapieco, C., Nuza, S. E., et al. 2015, *ApJL*, **800**, L4
- Dalla Vecchia, C., & Schaye, J. 2012, *MNRAS*, **426**, 140
- Davé, R., Anglés-Alcázar, D., Narayanan, D., et al. 2019, *MNRAS*, **486**, 2827
- Davé, R., Thompson, R., & Hopkins, P. F. 2016, *MNRAS*, **462**, 3265
- Dubois, Y., & Teyssier, R. 2008, *A&A*, **477**, 79
- Emerick, A., Bryan, G. L., & Mac Low, M.-M. 2018, *ApJL*, **865**, L22
- Fielding, D., Quataert, E., & Martizzi, D. 2018, *MNRAS*, **481**, 3325
- Forbes, J. C., Krumholz, M. R., & Speagle, J. S. 2019, *MNRAS*, **487**, 3581
- Gatto, A., Walch, S., Naab, T., et al. 2017, *MNRAS*, **466**, 1903
- Girichidis, P., Naab, T., Hanasz, M., & Walch, S. 2018, *MNRAS*, **479**, 3042
- Gurvich, A. B., Faucher-Giguère, C.-A., Richings, A. J., et al. 2020, *MNRAS*, **498**, 3664
- Harris, C. R., Millman, K. J., van der Walt, S. J., et al. 2020, *Natur*, **585**, 357
- Heckman, T. M., Alexandroff, R. M., Borthakur, S., Overzier, R., & Leitherer, C. 2015, *ApJ*, **809**, 147
- Heckman, T. M., Lehnert, M. D., Strickland, D. K., & Armus, L. 2000, *ApJS*, **129**, 493
- Hopkins, P. F., Grudić, M. Y., Wetzel, A., et al. 2020, *MNRAS*, **491**, 3702
- Hopkins, P. F., Quataert, E., & Murray, N. 2012, *MNRAS*, **421**, 3522
- Hopkins, P. F., Wetzel, A., Kereš, D., et al. 2018, *MNRAS*, **480**, 800
- Hoyer, S., & Hamman, J. 2017, *JORS*, **5**, 10
- Hu, C.-Y. 2019, *MNRAS*, **483**, 3363
- Hunter, J. D. 2007, *CSE*, **9**, 90
- Keller, B. W., Wadsley, J., Benincasa, S. M., & Couchman, H. M. P. 2014, *MNRAS*, **442**, 3013
- Kim, C.-G., & Ostriker, E. C. 2015, *ApJ*, **802**, 99
- Kim, C.-G., & Ostriker, E. C. 2017, *ApJ*, **846**, 133
- Kim, C.-G., & Ostriker, E. C. 2018, *ApJ*, **853**, 173
- Kim, C.-G., Ostriker, E. C., Somerville, R. S., et al. 2020, *ApJ*, **900**, 61
- Koyama, H., & Inutsuka, S.-I. 2002, *ApJL*, **564**, L97
- Kroupa, P. 2001, *MNRAS*, **322**, 231
- Lehnert, M. D., Heckman, T. M., & Weaver, K. A. 1999, *ApJ*, **523**, 575
- Leitherer, C., Schaerer, D., Goldader, J. D., et al. 1999, *ApJS*, **123**, 3
- Leroy, A. K., Walter, F., Martini, P., et al. 2015, *ApJ*, **814**, 83
- Li, M., & Bryan, G. L. 2020, *ApJL*, **890**, L30
- Li, M., Bryan, G. L., & Ostriker, J. P. 2017, *ApJ*, **841**, 101
- Martin, C. L. 2005, *ApJ*, **621**, 227
- Martini, P., Leroy, A. K., Mangum, J. G., et al. 2018, *ApJ*, **856**, 61
- McKinney, W. 2010, in Proc. 9th Python in Science Conf., ed. S. van der Walt & J. Millman (Austin, TX: SciPy), 56
- Melso, N., Bryan, G. L., & Li, M. 2019, *ApJ*, **872**, 47
- Motwani, B., Genel, S., Bryan, G. L., et al. 2020, arXiv:2006.16314
- Muratov, A. L., Kereš, D., Faucher-Giguère, C.-A., et al. 2015, *MNRAS*, **454**, 2691
- Naab, T., & Ostriker, J. P. 2017, *ARA&A*, **55**, 59
- Nelson, D., Pillepich, A., Springel, V., et al. 2019, *MNRAS*, **490**, 3234
- Oppenheimer, B. D., & Davé, R. 2006, *MNRAS*, **373**, 1265
- Pandya, V., Somerville, R. S., Anglés-Alcázar, D., et al. 2020, arXiv:2006.16317
- Perez, F., & Granger, B. E. 2007, *CSE*, **9**, 21
- Pillepich, A., Nelson, D., Springel, V., et al. 2019, *MNRAS*, **490**, 3196
- Pillepich, A., Springel, V., Nelson, D., et al. 2018, *MNRAS*, **473**, 4077
- Rupke, D. 2018, *Galax*, **6**, 138
- Schneider, E. E., Ostriker, E. C., Robertson, B. E., & Thompson, T. A. 2020, *ApJ*, **895**, 43
- Smith, M. C., Bryan, G. L., Somerville, R. S., et al. 2020, arXiv:2009.11309
- Somerville, R. S., & Davé, R. 2015, *ARA&A*, **53**, 51
- Somerville, R. S., Popping, G., & Trager, S. C. 2015, *MNRAS*, **453**, 4337
- Springel, V., & Hernquist, L. 2003, *MNRAS*, **339**, 289
- Stone, J. M., & Gardiner, T. 2009, *NewA*, **14**, 139
- Stone, J. M., Gardiner, T. A., Teuben, P., Hawley, J. F., & Simon, J. B. 2008, *ApJS*, **178**, 137
- Strickland, D. K., Heckman, T. M., Colbert, E. J. M., Hoopes, C. G., & Weaver, K. A. 2004, *ApJS*, **151**, 193
- Sun, J., Leroy, A. K., Ostriker, E. C., et al. 2020, *ApJ*, **892**, 148
- Sutherland, R. S., & Dopita, M. A. 1993, *ApJS*, **88**, 253
- Tollet, É., Cattaneo, A., Macciò, A. V., Dutton, A. A., & Kang, X. 2019, *MNRAS*, **485**, 2511
- van der Velden, E. 2020, *JOSS*, **5**, 2004
- Veilleux, S., Cecil, G., & Bland-Hawthorn, J. 2005, *ARA&A*, **43**, 769
- Veilleux, S., Maiolino, R., Bolatto, A. D., & Aalto, S. 2020, *A&ARv*, **28**, 2
- Vijayan, A., Kim, C.-G., Armillotta, L., Ostriker, E. C., & Li, M. 2020, *ApJ*, **894**, 12
- Virtanen, P., Gommers, R., Oliphant, T. E., et al. 2020, *NatMe*, **17**, 261
- Vogelsberger, M., Genel, S., Sijacki, D., et al. 2013, *MNRAS*, **436**, 3031